Hollow CaTiO$_3$ cubes modified by La/Cr co-doping for efficient photocatalytic hydrogen production

Ruinan Wang[a], Shuang Ni[b], Gang Liu[c], Xiaoxiang Xu[a],*

[a] *Shanghai Key Lab of Chemical Assessment and Sustainability, School of Chemical Science & Engineering, Tongji University, 1239 Siping Road, Shanghai 200092, China*
[b] *Science and Technology on Plasma Physics Laboratory, Laser Fusion Research Center, China Academy of Engineering Physics, Mianyang 621900, China*
[c] *Shenyang National laboratory for Materials Science, Institute of Metal Research, Chinese Academy of Science, 72 Wenhua Road, Shenyang 110016, China*

ARTICLE INFO

ABSTRACT

In this work, we have applied microstructure management and doping techniques to conventional wide band gap semiconductor CaTiO$_3$ with the aim to improve its light absorption and photocatalytic activity. A series of La/Cr co-doping hollow CaTiO$_3$ cubes have been successfully prepared by a template-free hydrothermal method. Their crystal structures, microstructures, optical absorption and photocatalytic hydrogen production have been systematically investigated. Our results suggest that hollow CaTiO$_3$ owns a higher light absorption than solid one and demonstrates a much better photocatalytic activity both under full range ($\lambda \geq 250$ nm) and visible light illumination ($\lambda \geq 400$ nm). These improvements probably originate from the peculiar hollow microstructures that increase photon-matter interactions and shorten the charge migration pathways. The photocatalytic activity for hydrogen production has been further studied by varying the La/Cr content in CaTiO$_3$. An optimal doping point at 5% La/Cr doping level has been reached for full range illumination with apparent quantum efficiency approaching ~2.41%. Nevertheless, the activity under visible light illumination shows a clear dependence on doping level with highest apparent quantum efficiency ~0.40% at 20% La/Cr doping level. DFT calculations reveal the critical role of Cr in forming a new spin-polarized valence band inside the original band gap of CaTiO$_3$ therefore is responsible for band gap reduction and visible light photocatalysis. This work here highlights the importance of microstructure control to the photocatalytic performance and shall shed a light on the design and development of efficient photocatalytic materials/systems.

1. Introduction

How to fulfil the ever-growing energy demand of our modern society is one of the premier targets for this century since current fossil-fuel based economy is not sustainable in essence, let alone various environmental issues associated with fossil fuel usage. There is now a worldwide agreement on searching/developing clean and renewable energy resources that can ultimately relieve us from fossil fuel reliance. In this regard, photocatalytic water splitting into hydrogen and oxygen, with the aid of solar energy, has been considered as a promising means to set up a sustainable energy infrastructure, not only because hydrogen is a clean energy vector but also because solar insolation is inexhaustible and is easily accessible worldwide [1–8]. Ever since the report of photo-electrochemical water splitting on titanium dioxide (TiO$_2$) in 1972 [9], great efforts have been devoted to the design and the development of new photocatalytic materials or systems yet very few compounds demonstrate photocatalytic activity high enough to warrant commercial interest. In general, the catalytic activity of a

semiconductor photocatalyst is a function of various parameters, such as crystallinity, defects, microstructures etc. Control of these parameters has been an effective way to tailor the photocatalytic activity of a particular semiconductor compound. For example, tetrahedral shaped Ag$_3$PO$_4$ submicro-crystals exhibit higher photocatalytic activities than normal Ag$_3$PO$_4$ particles for the degradation of organic contaminants under visible light irradiation [10]. Several approaches have been developed to fabricate architectures assembled with peculiar nanostructures by the assistance of templates and/or surfactants [11–13]. To avoid the complicated operations using templates, template-free methods with a few steps are highly welcome [14–16]. Along with microstructure management, a number of strategies such as dye sensitizing [17], nitridizing/sulfurizing [18–23], doping with foreign elements [24–26] etc., have been developed to extend the light absorption of wide band gap semiconductors. Among these strategies, doping with foreign atoms has been adopted as the most simple and effective method to enhance the light sensitivity of a semiconductor. This normally involves the formation of additional bands/energy levels within

---

* Corresponding author.
 E-mail address: xxxu@tongji.edu.cn (X. Xu).

the intrinsic band gaps of these compounds, which could significantly reduce the threshold of photon absorption [26]. It is known that metal oxides with perovskite-type structure (ABO_3) often show promising catalytic activity and their structures are extremely flexible and tolerant to cationic and anionic replacements. Applying doping strategies to these perovskites have witnessed a number of successes in improving the photocatalytic activities. For instance, recent reports have showed that Cr seems to be the most simple and cost-effective dopant for $SrTiO_3$ in extending its superior photocatalytic activities into visible light region [27,28].

In this work, we applied both microstructure control and doping strategies to perovskite compound $CaTiO_3$. We successfully synthesized hollow $CaTiO_3$ cubes modified by La/Cr co-doping via a facile template-free hydrothermal method. Their peculiar microstructures are found to be beneficial for light absorption due to enhanced reflection steps, which in turn contributes to a higher photocatalytic performance with respect to normal $CaTiO_3$. The photocatalytic activity of these hollow $CaTiO_3$ cubes was further optimized by adjusting the La/Cr co-doping levels. The microstructure manipulation combined with doping techniques in this study highlights an effective means to boost photocatalytic activity of conventional wide band gap semiconductors.

2. Experimental

2.1. Synthesis

La/Cr co-doped $CaTiO_3$ hollow cubes were synthesized according to previous reports with some modifications [16]. In a typical synthesis of $Ca_{0.80}La_{0.20}Ti_{0.80}Cr_{0.20}O_3$, 0.5725 g $Ca(NO_3)_2 \cdot 4H_2O$ (Aladdin, 99.0%), 0.2624 g $La(NO_3)_3 \cdot 6H_2O$ (Aladdin, 99.0%), 0.2425 g $Cr(NO_3)_3 \cdot 9H_2O$ (Aladdin, 99.0%) were dissolved in 3 ml deionized water according to the stoichiometric ratios. 57 ml polyethylene glycol-200 (PEG-200) was then added to above solution with sonication to promote dissolution. Subsequently, 0.792 ml titanium *n*-butoxide (Aladdin, 99.0%, TNB) were added dropwisely to the solution under magnetic stirring. All cations in the solution were then precipitated by adding 66 mmol sodium hydroxide (Aladdin, 96.0%) under magnetic stirring. The precipitates were transferred into a Teflon-lined stainless steel autoclave for hydrothermal treatment at 180 °C for 15 h. The resulting powders were separated by centrifuging and washed with ethanol (twice), diluted acetic acid (10 vol%, twice), and distilled water until pH reached 7 and dried in an oven at 80 °C for 12 h. The La/Cr co-doping levels were simply controlled by adjusting initial $La(NO_3)_3 \cdot 6H_2O$ and $Cr(NO_3)_3 \cdot 9H_2O$ content. These samples were labeled as Hollow. Normal La/Cr co-doped $CaTiO_3$ was also synthesized for comparison purpose: appropriate amounts of $Ca(NO_3)_2 \cdot 4H_2O$ (Aladdin, 99%), $La(NO_3)_3 \cdot 6H_2O$ (Aladdin, 99.0%), $Cr(NO_3)_3 \cdot 9H_2O$ (Aladdin, 99.0%) were dissolved in 15 ml deionized water to form a transparent solution. Proper amounts of titanium isopropanol (Aladdin, 95%, TIP) ethanol solution were then added slowly to above solution according to stoichiometric ratio. All cations in the solution were precipitated by adding 10 ml 10 M NaOH solution to form slurry. The slurry was transferred into a Teflon-lined stainless steel autoclave for hydrothermal treatment at 180 °C for 15 h. The powders formed were then washed with deionized water until pH reaches 7 and were dried in an oven at 80 °C for 12 h. These samples were labeled as Normal.

2.2. Methods for analysis

Crystal structure and phase composition were examined by using X-ray powder diffraction (XRD) techniques (Bruker D8 Focus diffractometer). The incident radiations were Cu $K_{\alpha1}$ (λ = 1.5406 Å) and Cu $K_{\alpha2}$ (λ = 1.5444 Å), respectively. The step size for data collection was 0.01° with a collection time of 0.1s at each step. The General Structure Analysis System (GSAS) software package was applied to perform Rietveld refinement on the data collected [29]. Microstructures

compositions of all samples were examined using a field emission scanning electron microscope (Hitachi S4800) equipped with a Mica energy dispersive X-ray spectroscopy (EDS) analysis system and a transmission electron microscope (JEOL JEM-2100). Surface conditions and binding energy of constitutional elements were analyzed using X-ray photoelectron spectroscopy (Thermo Escalab 250 with a monochromatic Al Kα X-ray source). All binding energies were referenced to the adventitious carbon C 1s peak at 284.7 eV [30]. Diffuse reflectance spectra were collected and analyzed on a UV–vis spectrophotometer (JASCO-V750) combined with the JASCO software suite. The reference non-absorbing material is $BaSO_4$ [31]. Specific surface areas were analysed using a Micromeritics instrument TriStar 3000 and were calculated via the Brunauer-Emmett-Teller (BET) model.

2.3. Photocatalytic hydrogen production

Photocatalytic activity of all specimens was performed in a top-irradiation-type reactor connected to a gas-closed circulation and evacuation system (Perfect Light, Labsolar-IIIAG). The typical gas pressure inside the reactor is 100 Pa. In a typical experiment, 100 mg sample powders were distributed in 100 ml aqueous solution, which was then transferred into the reactor and subjected to evacuation to remove air dissolved. Na_2SO_3 (0.05 M) was used as the sacrificial agent while Pt (1 wt%) was loaded as a co-catalyst to enhance the activity of photoreduction [32,33]. Pt was loaded onto the sample powders by a thermal deposition method [34–36]: appropriated amounts of H_2PtCl_6 aqueous solution was impregnated into sample powders which were then heated on a hot plate at 90 °C until dry. Thereafter, the temperature was raised to 180 °C for 2 h to fully convert H_2PtCl_6 into Pt nanoparticles. The solution is irradiated by using a 500 W high-pressure mercury lamp (NBeT, Merc-500) as the light source. The visible light illumination was produced by filtering the output of the lamp with a UV cut-off filter ($\lambda \geq 400$ nm). The photon flux of the lamp is gauged using a quantum meter (Apogee MP-300). A typical emission spectrum of the mercury lamp used in this work is shown in Fig. S1. The recorded photon flux is ~1543.9 µmol m^{-2} s^{-1} for full range irradiation ($\lambda \geq 250$ nm) and ~796.5 µmol m^{-2} s^{-1} for visible light irradiation ($\lambda \geq 400$ nm). Monochromic light irradiation was produced by filtering the output of the lamp with corresponding bandpass filters. The gas component within the reactor was then analyzed using an on-lined gas chromatograph (TECHCOMP, GC7900) with a thermal conductivity detector (5 Å molecular sieve columns and Ar carrier). The apparent quantum efficiency is then calculated using following equation:

Apparent quantum efficiency = 2 × mol of hydrogen production per hour/moles of photon flux per hour × 100%

2.4. Theoretical calculation

Theoretical calculations were performed using the density functional theory (DFT) implemented in the Vienna Ab initio Simulation Package (VASP) [37]. The Perdew, Burke, and Ernzerhof (PBE) exchange-correlation functional within the generalized gradient approximation (GGA) [38] and the projector augmented-wave pseudopotential were applied [39]. Spin-polarization was also considered during calculation. An orthorhombic unit cell (a = 5.38 Å, b = 5.44 Å, c = 7.639 Å, $\alpha = \beta = \gamma = 90°$) was constructed for simulation. La/Cr co-doping was considered by assuming that 1 Ca atom and 1 Ti atom were replaced by 1 La atom and 1 Cr atom, respectively. There are 20 atoms in the unit cell (1 La, 3Ca, 1 Cr, 3 Ti and 12 O) and the doping level is 25%. All geometry structures were fully relaxed until the forces on each atom are less than 0.01 eV Å^{-1}. Static calculations were done with a 9 × 9 × 7 Monkhorst-Pack k-point grid.
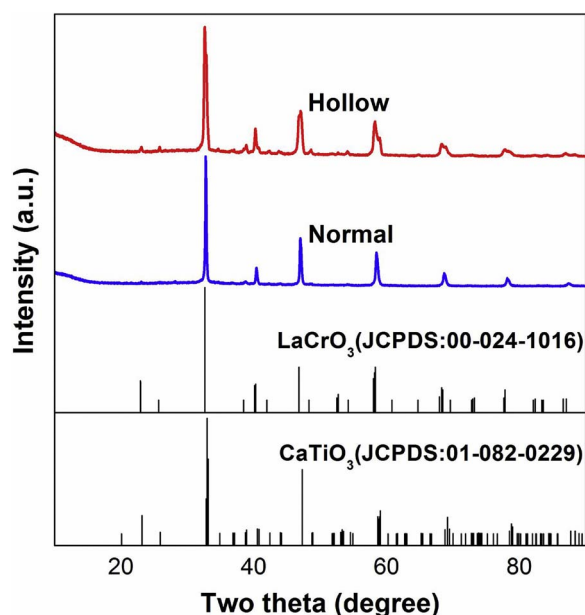
Fig. 1. X-ray powder diffraction patterns of as-prepared samples. Vertical bars of standard $CaTiO_3$ (JCPDS: 01-082-0229) and $LaCrO_3$ (JCPDS: 00-024-1016) patterns are also shown for visual inspections.

3. Results and discussion

3.1. Phase purity and crystal structure

X-ray powder diffraction patterns of as-prepared samples are displayed in Fig. 1. All samples exhibit similar patterns to pristine $CaTiO_3$ (JSPDS card number 01-082-0229) and can be indexed well using an orthorhombic symmetry, suggesting the formation of a single phase. The sharp diffraction peaks for both patterns suggest good crystallinity of sample powders. Super-lattice peaks due to cation ordering are not detected, implying that La/Cr dopants are randomly distributed in the $CaTiO_3$ crystal lattice. We then performed Rietveld refinement on the diffraction data. Typical refinement results of Hollow and Normal samples are displayed in Fig. S2 using an orthorhombic unit cell (space group *Pbnm*). Reasonable goodness-of-fit parameters (R_p, R_{wp} and χ^2) were only obtained by adding the constraints that Ca and La, Ti and Cr occupy the same crystallographic positions, respectively. The refined unit cell parameters are tabulated in Table 1. It can be seen from these data that Normal sample owns a more compact unit cell than Hollow one albeit their doping levels are kept the same.

3.2. Microstructures

Microstructures were then inspected using a field emission scanning electron microscopy (FESEM). FESEM images suggest that sample synthesized with PEG-200 is composed of cube-like particles with size ranging from hundreds of nanometers to a few microns (Fig. 2a and b). Interestingly, concaved surface can be clearly identified for these particles, implying that there is probably a pressure alteration between the inner and outer part of these cubes during their formation. On the contrary, sample prepared under normal conditions simply contains featureless granules with size about a few hundred nanometers (Fig. 2c

and d). Such a large dissimilarity between these two samples indicates the functionality of PEG-200 and amounts of water during the crystal growth procedure of $CaTiO_3$. These observations are consistent with previous report on the preparation of hollow $CaTiO_3$ and can be explained by the following mechanism: the presence of PEG-200 and small amounts of water induces a higher crystallinity at the surface than the inner part of nanocube assemblies at the initial hydrothermal process (Fig. S3) [16]. Further Ostwald ripening process at the inner part of nanocube assemblies leaves empty space inside therefore contributing to the formation of hollow cubes of $CaTiO_3$. The concaved surface is due to a density change during Ostwald ripening process which causes a pressure difference between the surface and the inner part of hollow cubes (Fig. S5) [16]. STEM-EDX element mapping measurements were also performed on Hollow sample $Ca_{0.80}La_{0.20}Ti_{0.80}Cr_{0.20}O_3$ (x = 0.2). It can be seen from mapping images that all constituent elements are homogeneously distributed, confirming that La/Cr dopants have been successfully doping into the crystal structure of $CaTiO_3$ (Fig. S4).

Microstructures of individual cube-like particle were further analyzed under transmission electron microscopy conditions (TEM). It can be seen from Fig. 3a that the cube-like particles are essentially hollow and the thickness of the cube wall is about 100 nanometers. Further analysis under HRTEM conditions suggests that the hollow cube is a single crystal with exposure of (004) lattice plane. These results are also comparable to previous reports. The variation on particle size of these cubes is probably due to the involvement of La/Cr dopants during synthesis that modifies the surface energy.

3.3. UV-vis spectroscopy

The color of both sample powders is yellow, presumably due to La/Cr dopants. Nevertheless, Hollow samples exhibit slightly deeper color even though both samples have the same doping level. This is confirmed from their UV–vis absorption spectra in Fig. 4. It can be seen from the spectra that Hollow sample has a higher light absorbance in both UV and visible region. It has been pointed out that the absorption band between 350–510 nm is attributed to metal to metal charge transfer (MMCT), i.e. $Cr^{3+} \rightarrow Ti^{4+}$ ($Cr^{3+} + Ti^{4+} \rightarrow Cr^{4+} + Ti^{3+}$) while the absorption peak centered around 620 nm is typical *d-d* transitions of Cr^{3+} in octahedral crystal field [40,41]. Since the doping level and the crystal structure of both samples are the same, the enhancement of light absorption is presumably due to the microstructures as will be explained in the following section. It is known that MMCT governs the photocatalytic activity of La/Cr co-doped $CaTiO_3$ under visible light illumination (pristine $CaTiO_3$ is only UV active). Microstructures of Hollow sample are therefore beneficial to photocatalytic performance as they enhance light absorption.

3.4. X-ray photoelectron spectroscopy and surface compositions

The surface nature and binding energy of constitutional elements were then examined by X-ray photoelectron spectroscopy (XPS). Binding energy of core-level electrons of O, Ti and Cr is plotted in Fig. 5. All of the energy signals are referenced to adventitious C 1s peak at 284.7 eV [30]. Overlapping peaks are unfolded by applying different Gaussian functions. The O 1s state contains three overlapped peaks centered at around 529 eV, 531 eV and 533 eV, assignable to the lattice oxygen anion, surface OH^- groups and carbonate species respectively [27,42]. The Ti 2p state contains two separated peaks at about 459 eV

Table 1
Space group, unit cell parameters, BET surface area and band gap values of samples prepared, standard deviations are included in parenthesis.

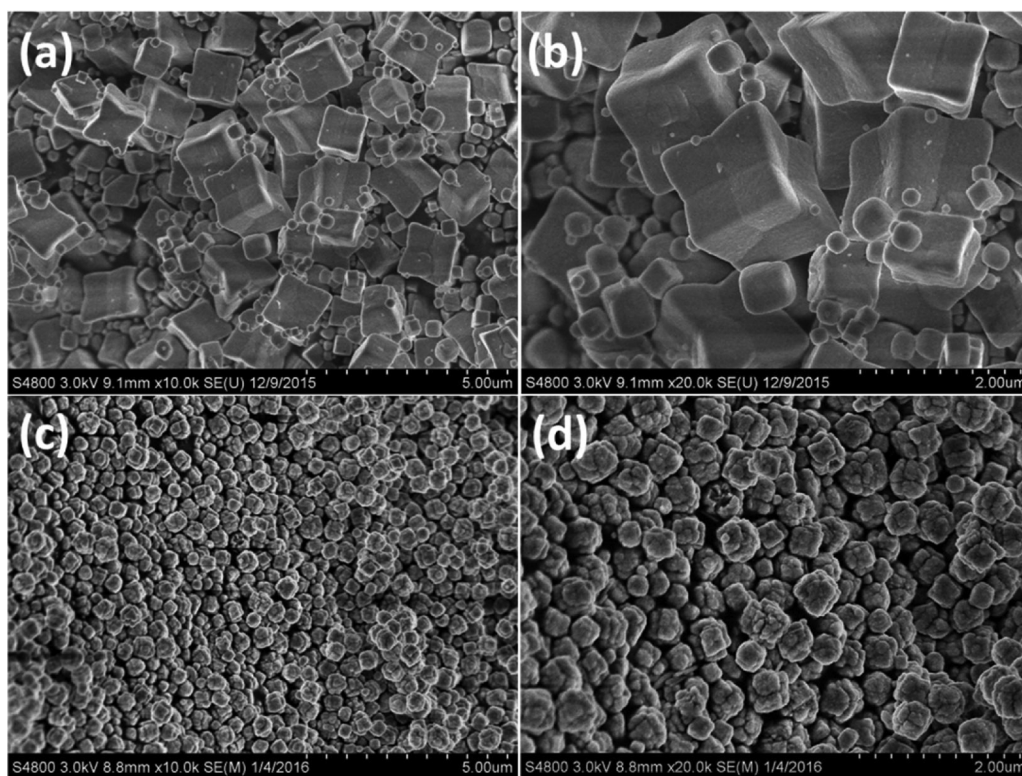| sample	Space group	a/Å	b/Å	c/Å	V/Å^3	BET surface area (m^2 g^{-1})	Band gap (eV)
Hollow	*Pbnm*	5.4487(2)	5.5000(2)	7.7733(6)	232.95(1)	9.51	2.48(5)
Normal	*Pbnm*	5.4551(3)	5.4676(4)	7.7240(8)	230.38(1)	12.26	2.49(8)

Fig. 2. Field emission scanning electron microscopy images of samples prepared by different routes: (a) and (b) hydrothermal method with PEG-200 (Hollow samples); (c) and (d) hydrothermal method without PEG-200 (Normal samples).
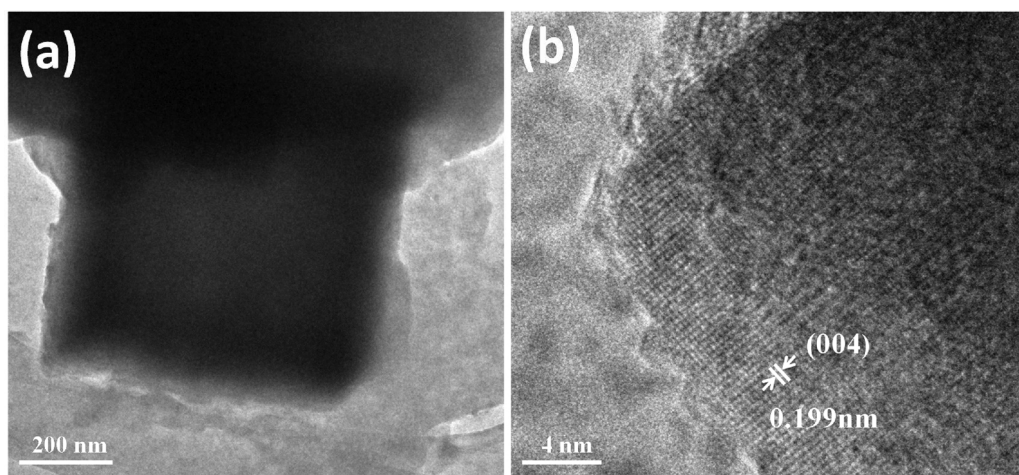

Fig. 3. Transmission electron microscopy (TEM) image (a) and high-resolution TEM (HRTEM) image (b) of cube-like particles.

and 464 eV, attributable to Ti $2p_{3/2}$ and Ti $2p_{1/2}$ states of Ti^{4+} species due to spin-orbital splitting, respectively. The Cr 2p state contains two overlapped peaks centered at around 577 eV and 587 eV, corresponding to Cr $2p_{3/2}$ and Cr $2p_{1/2}$ states of Cr^{3+} species [43]. High oxidation state of Cr such as Cr^{6+} is not detected here and can be explained by the co-doping strategy in which charge of the whole crystal is properly balanced between $La_{Sr}^{\cdot}$ and Cr_{Ti}' dopants [28].

3.5. Photocatalytic hydrogen production

The photocatalytic properties of both samples were then evaluated by monitoring hydrogen evolution in presence of sodium sulfite aqueous solution (0.05 M) under different light illumination conditions. Control experiments were firstly carried out with one of the following items absent, i.e. photocatalyst, light illumination and sodium sulfite. No hydrogen was detected for 5 h under these conditions, thereby precluding any spontaneous reactions to produce hydrogen. Immediate

hydrogen evolution was detected once sample powders were illuminated in the presence of sodium sulfite aqueous solution, confirming real photocatalytic reactions. The temporal photocatalytic hydrogen production for both samples under full range illumination ($\lambda \geq 250$ nm) is presented in Fig. 6a. It is clear from Fig. 6a that the activity of Hollow sample is about twice as much as that of Normal sample under full range illumination ($\lambda \geq 250$ nm). More interestingly, both samples exhibit photocatalytic hydrogen production under visible light illumination ($\lambda \geq 400$ nm) and their average hydrogen production rate is summarized in Fig. 6b. The average H$_2$ production rate of Hollow sample in this case is almost four fold higher than that of Normal sample, indicative of superior photocatalytic activity under visible light illumination. This is quite surprising as Hollow sample has a smaller surface area than Normal one (Table 1). Loading 1 wt% Pt significantly boosts the photocatalytic activity and Hollow sample without Pt loading exhibit even a better activity than Normal one loaded with 1 wt% Pt, furthering confirming the superior performance
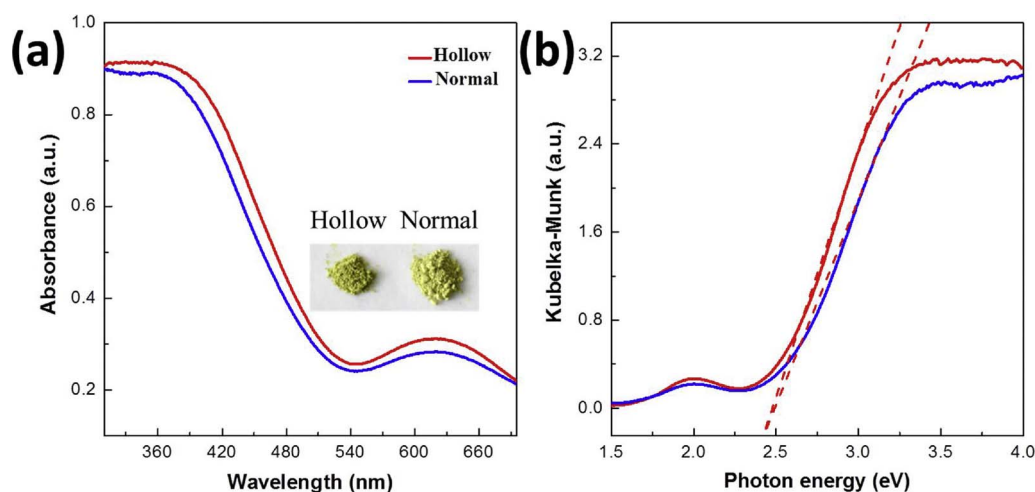
Fig. 4. (a) UV–vis light absorption spectra (converted from diffuse reflectance spectra) of the freshly prepared samples, photograph of sample powders is inserted, (b) Kubelka-Munk transformation of the diffuse reflectance data.
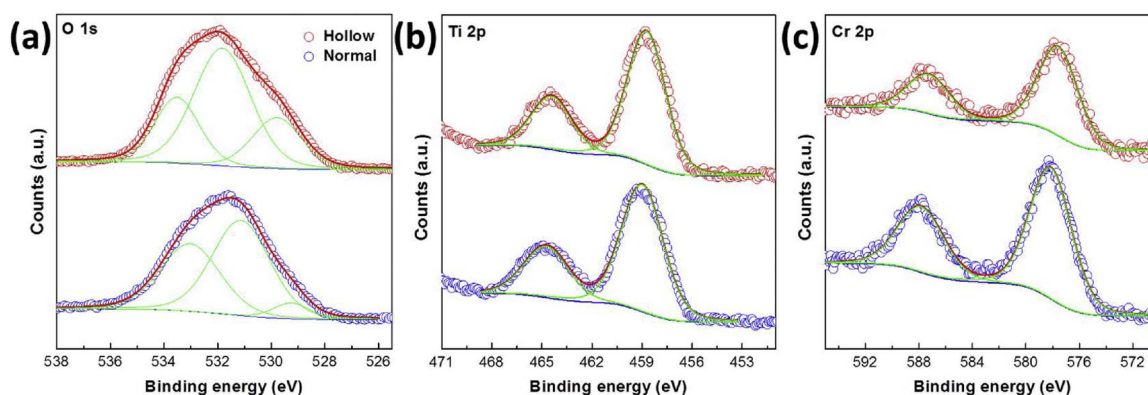

Fig. 5. XPS spectra of freshly as-prepared samples at a co-doping level of 20%: (a) O 1s state, (b) Ti 2p state, (c) Cr 2p state.
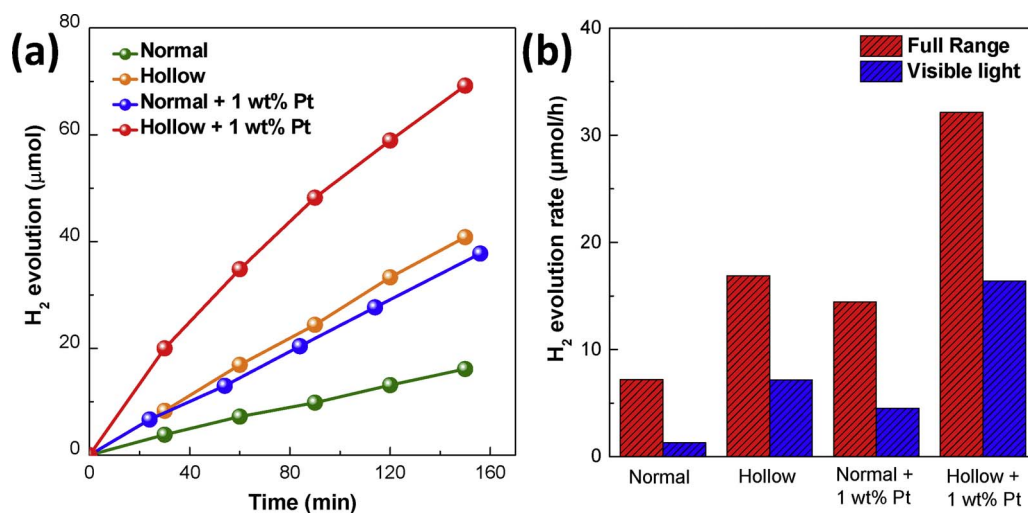

Fig. 6. (a) Photocatalytic hydrogen production of samples under full range irradiation ($\lambda \geq 250$ nm) in sodium sulfite aqueous solution (0.05 M), (b) average photocatalytic hydrogen production rate under full range irradiation ($\lambda \geq 250$ nm) and visible light irradiation ($\lambda \geq 400$ nm).

of this sample.

3.6. Theoretical calculations

For better understanding the role of La/Cr dopants to the photocatalytic activity of $CaTiO_3$, we then performed theoretical calculation on the electronic structure of La/Cr co-doped $CaTiO_3$ using density functional theory (DFT). The calculated band structure and density of states (DOS) near Fermi levels are illustrated in Fig. 7. La/Cr co-doped $CaTiO_3$ maintains the semiconductivity with a calculated band gap

about 0.34 eV. This value is much smaller than experimental one from UV–vis spectra and is attributed to the drawbacks of the generalized gradient approximation (GGA) method for underestimating the band separations [44]. Nevertheless, the calculated results offer qualitative information. It can be seen from Fig. 7 that a spin-polarized valence band (SPVB), which originated from Cr 3d orbitals, appears inside the intrinsic band gap of $CaTiO_3$ [45]. Therefore, the decreased band gap of La/Cr co-doped $CaTiO_3$ is due to this newly formed valence band (VB) that considerably reduces the threshold for electron excitations. Considering the factor that the conduction band (CB) has major
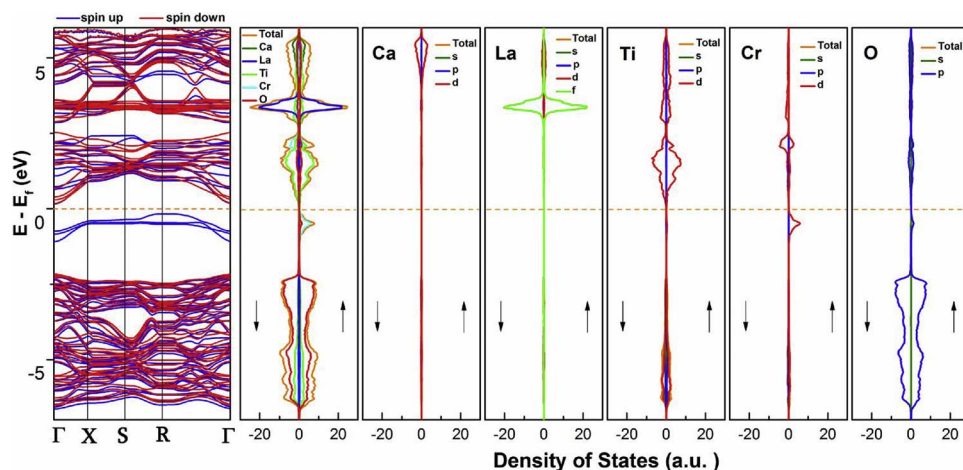
Fig. 7. Calculated band structure, total density of states (DOS), and partial density of states (PDOS) of constituent elements for $Ca_{0.80}La_{0.20}Ti_{0.80}Cr_{0.20}O_3$, spin directions are indicated by arrows ($\downarrow\uparrow$) and the Fermi level is marked by the dotted orange lines. (For interpretation of the references to color in this figure legend, the reader is referred to the web version of this article.)
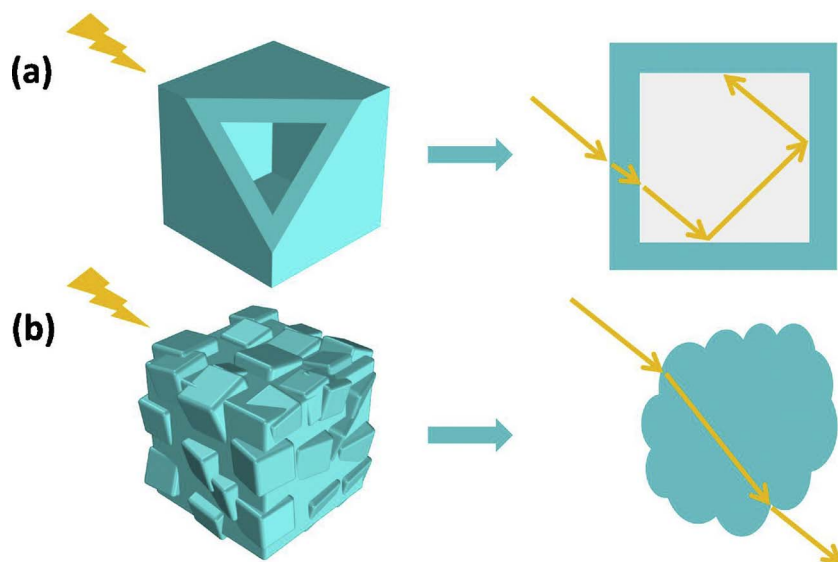

Fig. 8. Schematic representations of light reflections and refractions in (a) Hollow sample and (b) Normal sample, reflections at the surface are omitted for clarity.
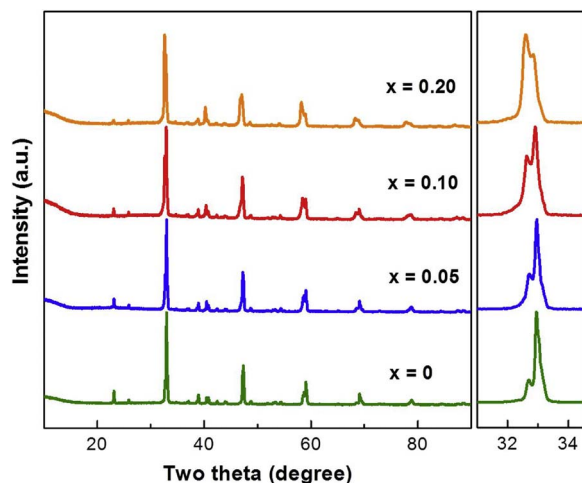

Fig. 9. X-ray powder diffraction patterns of as-prepared samples $Ca_{1-x}La_xTi_{1-x}Cr_xO_3$ (x = 0, 0.05, 0.10, 0.20).

contribution from Ti 3d orbitals and photons have no spin, the visible light photocatalytic activity of La/Cr co-doped $CaTiO_3$ is mainly due to electron excitation from SPVB to upper CB, i.e. $Cr^{3+} \rightarrow Ti^{4+}$ charge transfer (MMCT). It is worth noting that La contributes neither to the conduction minimum nor to the valence band maximum therefore acts
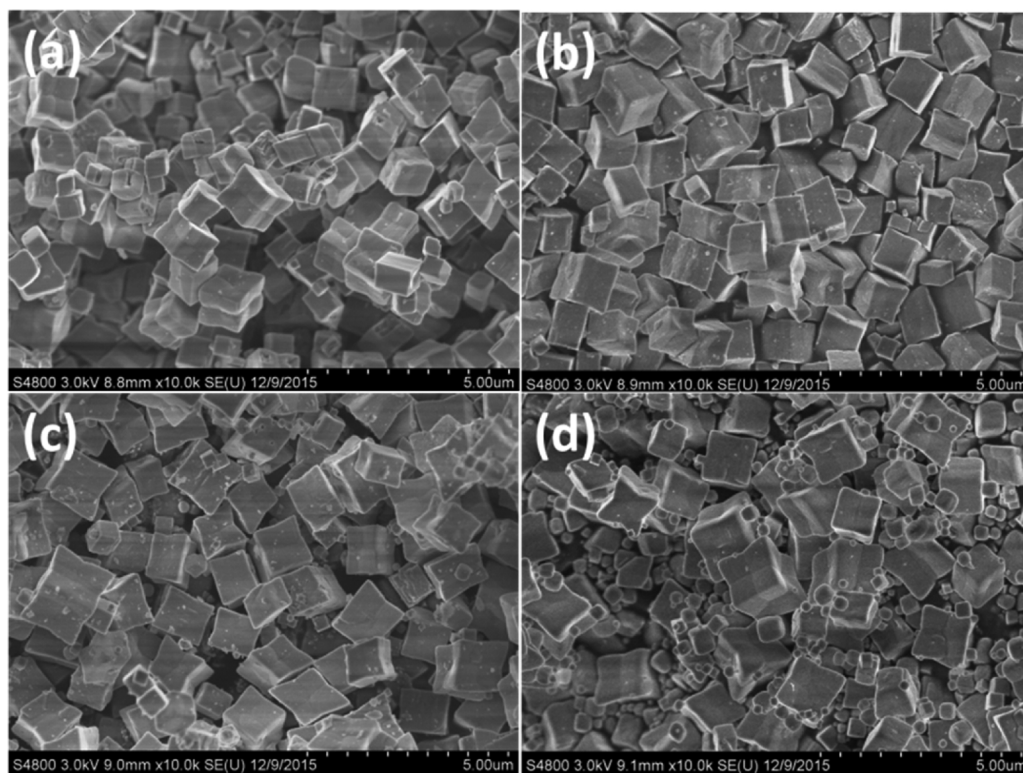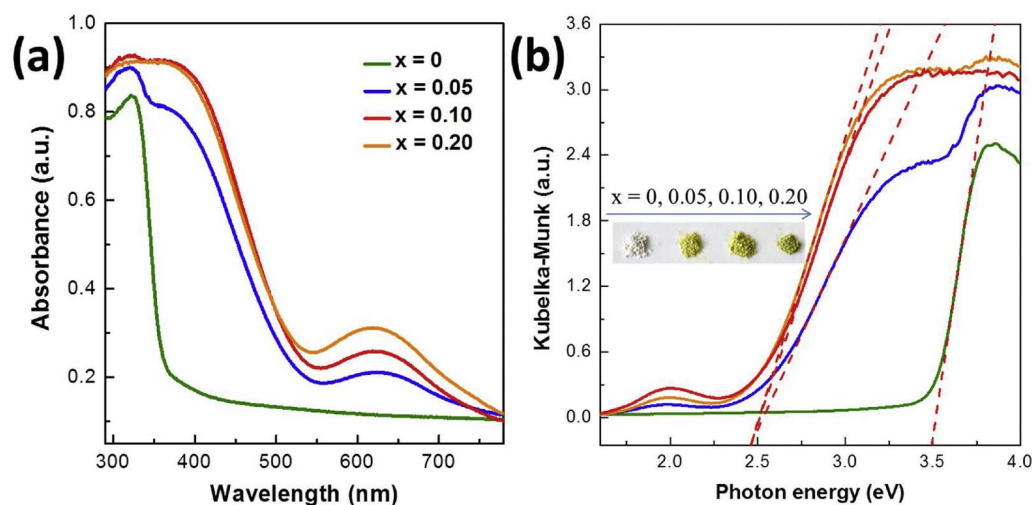
as a charge balancer to maintain the charge neutrality of the compound during Cr doping [46,47].

We then tentatively explain the dissimilar photocatalytic activity observed for Hollow and Normal samples. In case of Hollow sample, the empty inner part of the cube-like particles offers more interfaces that would considerably increase chance of light reflections. The extra light reflections enhance the light absorption due to the higher rate of photon-matter contact compared to solid sample (Fig. 8). Hollow sample thereby has a higher light absorption and increased photo-generated charges. Furthermore, considering the fact that the thickness of the cube wall is around 100 nm, all photo-generated charges will be easy to migrate to the surface for photocatalytic reactions even if the particle size is as large as several microns. This is not the case for Normal sample in which charges generated deeply inside the particles will have to take a long trip to reach the surface upon which severe charge recombination events might occur. Thereby, Hollow sample exhibits a better photocatalytic activity than Normal one. Besides, as long wavelength photons have longer absorption/penetration depth than short wavelength photons, the peculiar hollow cube micro-structures is therefore more efficient in absorbing long wavelength photons. This explains why activity enhancement is more pronounced under visible light illumination (four fold enhancement) than full range illumination (two fold enhancements) between Hollow sample and Normal one.

Table 2

Space group, unit cell parameters, BET surface area and band gap values of samples prepared, standard deviations are included in parenthesis.

Sample	Space group	a/Å	b/Å	c/Å	V/Å^3	BET surface area (m^2 g^{-1})	Band gap (eV)
CaTiO$_3$	*Pbnm*	5.4029(1)	5.4749(1)	7.6697(1)	226.88(1)	5.37	3.51(5)
Ca$_{0.95}$La$_{0.05}$Ti$_{0.95}$Cr$_{0.05}$O$_3$	*Pbnm*	5.4063(2)	5.4770(2)	7.6785(2)	227.37(1)	14.69	2.49(2)
Ca$_{0.90}$La$_{0.10}$Ti$_{0.90}$Cr$_{0.10}$O$_3$	*Pbnm*	5.4285(4)	5.4953(4)	7.6946(5)	229.54(2)	9.72	2.48(2)
Ca$_{0.80}$La$_{0.20}$Ti$_{0.80}$Cr$_{0.20}$O$_3$	*Pbnm*	5.4487(2)	5.5000(2)	7.7733(6)	232.95(1)	9.51	2.50(2)

Fig. 10. Field emission scanning electron microscopy images of Ca$_{1-x}$La$_x$Ti$_{1-x}$Cr$_x$O$_3$: (a) x = 0, (b) x = 0.05, (c) x = 0.10, (d) x = 0.20.

Fig. 11. (a) UV–vis light absorption spectra (converted from diffuse reflectance spectra) of the freshly prepared samples Ca$_{1-x}$La$_x$Ti$_{1-x}$Cr$_x$O$_3$ (x = 0, 0.05, 0.10, 0.20) and (b) Kubelka-Munk transformation of the diffuse reflectance data, the photograph of sample powders is shown in the inset.

3.7. The effect of La/Cr co-doping levels

We then try to optimize the photocatalytic activity of Hollow sample by controlling the La/Cr co-doping levels. A series of La/Cr co-doped CaTiO$_3$, i.e. Ca$_{1-x}$La$_x$Ti$_{1-x}$Cr$_x$O$_3$ (x = 0, 0.05, 0.10, 0.20) were prepared with the same procedure by varying the initial La/Cr content. Their XRD patterns are displayed in Fig. 9. All samples exhibit similar patterns that can be indexed well by an orthorhombic symmetry, suggesting the formation of a single phase. There is an apparent peak shift towards low angles along with of La/Cr co-doping (Fig. 9 right), indicative of unit cell expansion during La/Cr substitution. We then performed Rietveld refinement on these diffraction data using an orthorhombic unit cell (space group *Pbnm*). Typical refinement results of Ca$_{0.80}$La$_{0.20}$Ti$_{0.80}$Cr$_{0.20}$O$_3$ are displayed in Fig. S2b. The refined unit cell
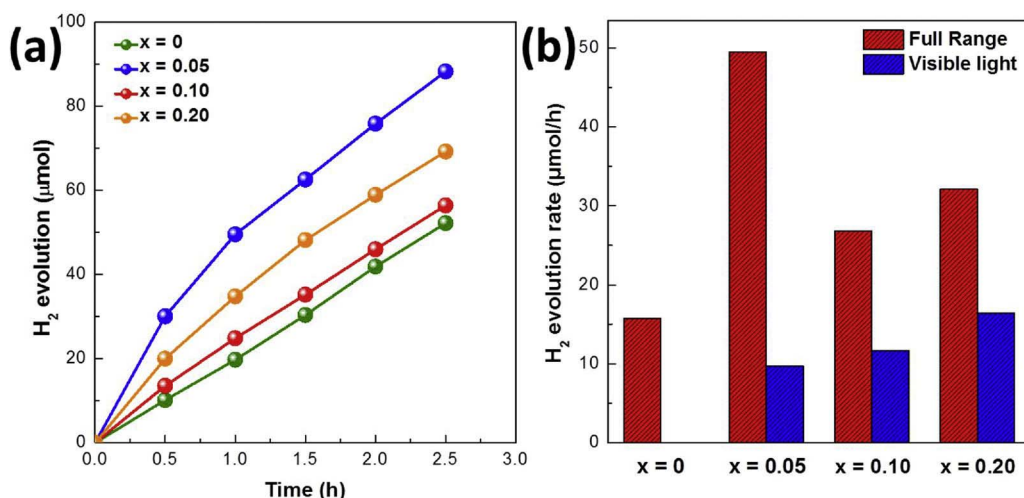
Fig. 12. (a) Photocatalytic hydrogen production of samples $Ca_{1-x}La_xTi_{1-x}Cr_xO_3$ (x = 0, 0.05, 0.10, 0.20) under full range irradiation ($\lambda \geq$ 250 nm) in sodium sulfite aqueous solution (0.05 M) and (b) average photocatalytic hydrogen production rate under full range irradiation ($\lambda \geq$ 250 nm) and visible light irradiation ($\lambda \geq$ 400 nm).
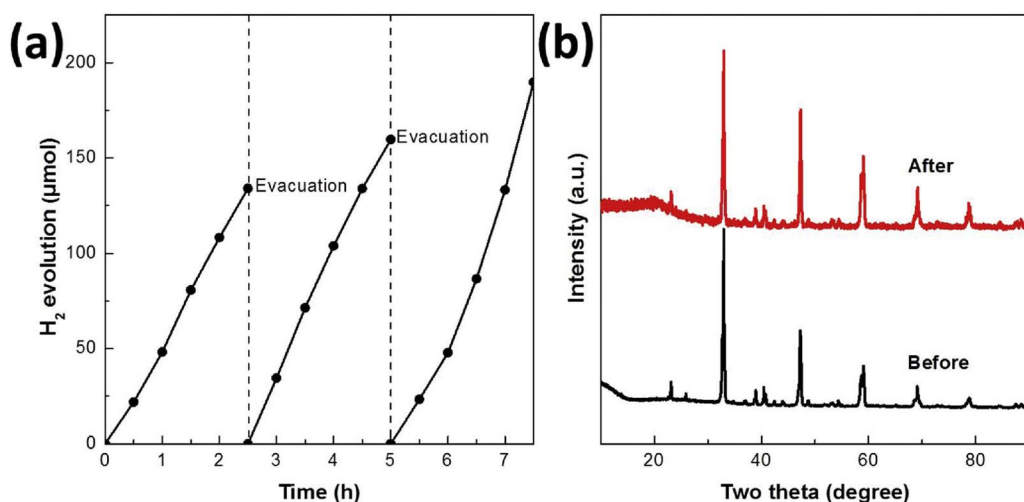

Fig. 13. (a) Repeated time courses of photocatalytic hydrogen production for $Ca_{0.95}La_{0.05}Ti_{0.95}Cr_{0.05}O_3$ under full range irradiation ($\lambda \geq$ 250 nm) in sodium sulfite aqueous solution (0.05 M) (Evacuation proceeds at every 2.5 h) and (b) XRD patterns for $Ca_{0.95}La_{0.05}Ti_{0.95}Cr_{0.05}O_3$ before and after photocatalytic reactions.

parameters are tabulated in Table 2. As can be seen from Table 2, unit cell parameters increase with increasing La/Cr co-doping levels as Cr^{3+} cations are slightly larger than Ti^{4+} cations at octahedron coordination (r_{Ti4+} = 0.605 Å, r_{Cr3+} = 0.615 Å), being consistent with Vegard's law. La here serves as a charge balancer which compensates the charge mismatch during Cr doping, i.e. $Cr'_{Ti} + La^{\bullet}_{Ca}$. The atomic compositions of these samples were then checked by using EDS techniques and are tabulated in Table S1. The atomic ratios of these samples are all in good accord to their nominal compositions.

The microstructures of freshly prepared sample powders were inspected using a field emission scanning electron microscope (Fig. 10). The photographs indicate that the microstructures of the samples are more or less affected by the La/Cr content in the specimens. Much narrow particle size distributions can be identified for those samples with low doping levels. Nevertheless, all samples exhibit cube-like particles with concaved surface, implying that the hollow features of these particles are maintained.

The color of these samples turns deeper along with La/Cr co-doping. Pristine $CaTiO_3$ is white therefore is a typical wide band gap semiconductor. Yellowish color appears for just 5% La/Cr co-doping, highlighting the effectiveness of La/Cr for improving light absorption. Their UV–vis spectra are illustrated in Fig. 11. Pristine $CaTiO_3$ has a clear absorption edge around 350 nm and no discernable absorption in the visible light region. The absorption edge is clearly red-shifted into visible light region with La/Cr co-doping. The MMCT absorption band is saturated quickly at a doping level of 10% and further increasing the doping level has no apparent contribution to this band except an

increase of d-d transition band. This corroborates the assignment of these bands as d-d transition band is controlled only by the Cr concentration while MMCT is governed both by Cr and Ti species. The gradual substitution of Ti with Cr decreases the Ti content in the sample which serves as a damping factor for MMCT. The yellowish color of these samples indicates that all Cr remains in trivalent state which would otherwise give violet appearance if high oxidation state Cr species such as Cr^{6+} exist. This is also confirmed by their XPS spectra that bonding energy of Cr 2p state belongs to Cr^{3+} species (Fig. S6).

The photocatalytic properties of these samples were then examined by monitoring the hydrogen evolution from sodium sulfite aqueous solution (0.05 M) under light illumination. The co-catalyst Pt loading was kept as the same (1 wt%). The temporal photocatalytic hydrogen production for all samples under full range illumination is presented in Fig. 12 and S7. It is clear from these figures that La/Cr co-doped samples all demonstrate a better activity than pristine $CaTiO_3$. The highest activity under full range irradiation ($\lambda \geq$ 250 nm) belongs to sample $Ca_{0.95}La_{0.05}Ti_{0.95}Cr_{0.05}O_3$, where more than 88.25 μmol of hydrogen was produced within 2.5 h. This value is more than 3 fold higher than pristine $CaTiO_3$, verifying the benefit of La/Cr co-doping. Further increasing La/Cr co-doping level leads to a slight decrease in the activity, which might be correlated with the decreased surface area (Table 2). Nevertheless, photocatalytic activity under visible light illumination has a clear dependence on the level of La/Cr co-doping. Their average hydrogen production rate is summarized in Fig. 12b and S7b. It can be seen from these figures that $Ca_{0.95}La_{0.05}Ti_{0.95}Cr_{0.05}O_3$ shows the highest averaged hydrogen production rate ~49.51 μmol h^{-1} under full range

illumination, corresponding to an apparent quantum efficiency of ~0.63%. However, the highest average hydrogen production rate under visible light illumination belongs to $Ca_{0.80}La_{0.20}Ti_{0.80}Cr_{0.20}O_3$, which gives a value of ~16.40 μmol h^{-1}, corresponding to an apparent quantum efficiency of ~0.40%. Its performance was further analyzed under monochromic light illumination. Action spectra of $Ca_{0.80}La_{0.20}Ti_{0.80}Cr_{0.20}O_3$ are illustrated in Fig. S8. AQE of $Ca_{0.80}La_{0.20}Ti_{0.80}Cr_{0.20}O_3$ shows a clear dependence on the wavelength of incident photons, confirming real photocatalytic processes.

The reproducibility of photocatalytic activity of these doped $CaTiO_3$ was checked by extending light illumination to several cycles. Fig. 13a illustrates the temporal photocatalytic hydrogen production of $Ca_{0.95}La_{0.05}Ti_{0.95}Cr_{0.05}O_3$ for 7.5 h with evacuation after every 2.5 h. Continuous hydrogen production was detected for the whole illumination period and the activity was gradually boosted. About 483.60 μmol H_2 was produced for the 7.5 h which exceeds the total amounts of catalyst used (354 μmol), confirming an efficient photocatalyst. The gradual enhancement in the activity can be explained by the surface activation in which more reaction sites were built during photocatalytic reactions. The AQE at final cycle approaches 2.41%. The stability of the sample after the reaction was further checked by XRD and the patterns remain the same before and after the reactions, verifying good stability of this photocatalyst (Fig. 13b).

4. Conclusions

We have successfully synthesized a series of La/Cr co-doped hollow $CaTiO_3$ via a template-free hydrothermal method. Their crystal structure, morphology, optical absorption and photocatalytic properties were thoroughly investigated. Our findings suggest that hollow $CaTiO_3$ owns a higher light absorption in comparison to solid one due to enhanced photon-matter interaction and a much better photocatalytic activity for hydrogen production both under full range and visible light illumination. Their photocatalytic activities were further optimized by altering the La/Cr content in $CaTiO_3$ and an optimal point at 5% La/Cr doping level was reached under full range illumination, which gave the highest AQE ~2.41%. Nevertheless, their photocatalytic activity under visible light illumination increased along with La/Cr incorporation, which gave the highest AQE ~0.40%. Theoretical calculations confirmed the critical role of Cr in forming a new SPVB insider the original band gap of $CaTiO_3$ therefore is responsible for band gap reduction and visible light photocatalytic activity. This work here signifies the usefulness of morphology management and doping techniques in improving the photocatalytic activity of conventional wide band gap semiconductor.

Acknowledgements

Appendix A. Supplementary data

Supplementary data associated with this article can be found, in the online version, at https://doi.org/10.1016/j.apcatb.2017.11.061.

References

[1] X. Xu, C. Randorn, P. Efstathiou, J.T. Irvine, Nat. Mater. 11 (2012) 595–598.
[2] Z. Yue, A. Liu, C. Zhang, J. Huang, M. Zhu, Y. Du, P. Yang, Appl. Catal. B-Environ. 201 (2017) 202–210.
[3] S.-S. Yi, J.-M. Yan, B.-R. Wulan, S.-J. Li, K.-H. Liu, Q. Jiang, Appl. Catal. B-Environ. 200 (2017) 477–483.
[4] A. Meng, J. Zhang, D. Xu, B. Cheng, J. Yu, Appl. Catal. B-Environ. 198 (2016) 286–294.
[5] D. Jiang, Z. Sun, H. Jia, D. Lu, P. Du, J. Mater. Chem. A 4 (2016) 675–683.
[6] Q. Li, X. Li, S. Wageh, A.A. Al-Ghamdi, J. Yu, Adv. Energy Mater. 5 (2015).
[7] M.M. Momeni, Y. Ghayeb, Z. Ghonchegi, Ceram. Int. 41 (2015) 8735–8741.
[8] M. Lv, Y. Wang, L. Lu, R. Wang, S. Ni, G. Liu, X. Xu, Phys. Chem. Chem. Phys. 18 (2016) 21491–21499.
[9] A. Fujishima, K. Honda, Nature 238 (1972) 37–38.
[10] H. Hu, Z. Jiao, H. Yu, G. Lu, J. Ye, Y. Bi, J. Mater. Chem. A 1 (2013) 2387–2390.
[11] W. Dong, B. Li, Y. Li, X. Wang, L. An, C. Li, B. Chen, G. Wang, Z. Shi, J. Phys. Chem. C 115 (2011) 3918–3925.
[12] J.B. Joo, Q. Zhang, I. Lee, M. Dahl, F. Zaera, Y. Yin, Adv. Funct. Mater. 22 (2012) 166–174.
[13] Y. Li, X. Cheng, X. Ruan, H. Song, Z. Lou, Z. Ye, L. Zhu, Nano Energy 12 (2015) 775–784.
[14] J. Li, S. Hietala, X. Tian, ACS Nano 9 (2014) 496–502.
[15] H. Zhan, X. Yang, C. Wang, J. Chen, Y. Wen, C. Liang, H.F. Greer, M. Wu, W. Zhou, Cryst. Growth Des. 12 (2012) 1247–1253.
[16] X. Yang, J. Fu, C. Jin, J. Chen, C. Liang, M. Wu, W. Zhou, J. Am. Chem. Soc. 132 (2010) 14279–14287.
[17] Z. Wang, W. Mao, H. Chen, F. Zhang, X. Fan, G. Qian, Catal. Commun. 7 (2006) 518–522.
[18] R. Asahi, T. Morikawa, T. Ohwaki, K. Aoki, Y. Taga, Science 293 (2001) 269–271.
[19] K. Maeda, T. Takata, M. Hara, N. Saito, Y. Inoue, H. Kobayashi, K. Domen, J. Am. Chem. Soc. 127 (2005) 8286–8287.
[20] Z. Lei, G. Ma, M. Liu, W. You, H. Yan, G. Wu, T. Takata, M. Hara, K. Domen, C. Li, J. Catal. 237 (2006) 322–329.
[21] H. Irie, Y. Watanabe, K. Hashimoto, J. Phys. Chem. B 107 (2003) 5483–5486.
[22] J. Liu, T. Hisatomi, G. Ma, A. Iwanaga, T. Minegishi, Y. Moriya, M. Katayama, J. Kubota, K. Domen, Energy Environ. Sci. 7 (2014) 2239–2242.
[23] F. Wu, M. Lv, X. Sun, Y. Xie, H. Chen, S. Ni, G. Liu, X. Xu, ChemCatChem 8 (2016) 615–623.
[24] J. Choi, H. Park, M.R. Hoffmann, J. Phys. Chem. C 114 (2009) 783–792.
[25] Q. Wang, T. Hisatomi, S.S.K. Ma, Y. Li, K. Domen, Chem. Mater. 26 (2014) 4144–4150.
[26] X. Sun, Y. Xie, F. Wu, H. Chen, M. Lv, S. Ni, G. Liu, X. Xu, Inorg. Chem. 54 (2015) 7445–7453.
[27] M. Lv, Y. Xie, Y. Wang, X. Sun, F. Wu, H. Chen, S. Wang, C. Shen, Z. Chen, S. Ni, Phys. Chem. Chem. Phys. 17 (2015) 26320–26329.
[28] P. Reunchan, S. Ouyang, N. Umezawa, H. Xu, Y. Zhang, J. Ye, J. Mater. Chem. A 1 (2013) 4221–4227.
[29] A. Lawson, A.C. Larson, M. Aronson, S. Johnson, Z. Fisk, P. Canfield, J. Thompson, R. Von Dreele, J. Appl. Phys. 76 (1994) 7049–7051.
[30] P. Van der Heide, X-ray Photoelectron Spectroscopy: an Introduction to Principles and Practices, John Wiley & Sons, 2011.
[31] G. Kortüm, W. Braun, G. Herzog, Angew. Chem. Int. Ed. 2 (1963) 333–341.
[32] X. Xu, G. Liu, A.K. Azad, Int. J. Hydrogen Energy 40 (2015) 3672–3678.
[33] X. Xu, G. Liu, C. Randorn, J.T. Irvine, Int. J. Hydrogen Energy 36 (2011) 13501–13507.
[34] H.M. Chen, Y.H. Xie, X.Q. Sun, M.L. Lv, F.F. Wu, L. Zhang, L. Li, X.X. Xu, Dalton Trans. 44 (2015) 13030–13039.
[35] H.M. Chen, X.Q. Sun, X.X. Xu, Electrochim. Acta 252 (2017) 138–146.
[36] X.X. Xu, M.L. Lv, X.Q. Sun, G. Liu, J. Mater. Sci. 51 (2016) 6464–6473.
[37] G. Kresse, J. Furthmüller, Phys. Rev. B 54 (1996) 11169.
[38] J.P. Perdew, K. Burke, M. Ernzerhof, Phys. Rev. Lett. 77 (1996) 3865.
[39] G. Kresse, D. Joubert, Phys. Rev. B 59 (1999) 1758.
[40] T. Ishii, H. Kato, A. Kudo, J. Photochem. Photobiol. A: Chem. 163 (2004) 181–186.
[41] U. Sulaeman, S. Yin, T. Sato, Appl. Catal. B: Environ. 105 (2011) 206–210.
[42] X. Xu, Y. Xie, S. Ni, A.K. Azad, T. Cao, J. Solid State Chem. 230 (2015) 95–101.
[43] A. Rahman, M. Mohamed, M. Ahmed, A. Aitani, Appl. Catal. A: Gen. 121 (1995) 203–216.
[44] H. Xiao, J. Tahir-Kheli, W.A. Goddard III, J. Phys. Chem Lett. 2 (2011) 212–217.
[45] X. Xu, M. Lv, X. Sun, G. Liu, J. Mater. Sci. 51 (2016) 6464–6473.
[46] X.Q. Sun, Y.H. Xie, F.F. Wu, H.M. Chen, M.L. Lv, S. Ni, G. Liu, X.X. Xu, Inorg. Chem. 54 (2015) 7445–7453.
[47] X.Q. Sun, X.X. Xu, Appl. Catal. B-Environ. 210 (2017) 149–159.